The Influence of WENO Schemes on Large-Eddy Simulations of a Neutral Atmospheric Boundary Layer

AARON WANG,[a] YING PAN,[a] AND PAUL M. MARKOWSKI[a]

[a] *The Pennsylvania State University, University Park, Pennsylvania*

(Manuscript received 2 February 2021, in final form 13 August 2021)

ABSTRACT: This work explores the influence of weighted essentially nonoscillatory (WENO) schemes on Cloud Model 1 (CM1) large-eddy simulations (LES) of a quasi-steady, horizontally homogeneous, fully developed, neutral atmospheric boundary layer (ABL). An advantage of applying WENO schemes to scalar advection in compressible models is the elimination of acoustic waves and associated oscillations of domain-total vertical velocity. Applying WENO schemes to momentum advection in addition to scalar advection yields no further advantage but has an adverse effect on resolved turbulence within LES. As a tool designed to reduce numerically generated spurious oscillations, WENO schemes also suppress physically realistic instability development in turbulence-resolving simulations. Thus, applying WENO schemes to momentum advection reduces vortex stretching, suppresses the energy cascade, reduces shear-production of resolved Reynolds stress, and eventually amplifies the differences between the surface-layer mean wind profiles in the LES and the mean wind profiles expected in accordance with the filtered law of the wall (LOTW). The role of WENO schemes in adversely influencing surface-layer turbulence has inspired a concept of anti-WENO (AWENO) schemes to enhance instability development in regions where energy-containing turbulent motions are inadequately resolved by LES grids. The success in reproducing the filtered LOTW via AWENO schemes suggests that improving advection schemes is a critical component toward faithfully simulating near-surface turbulence and dealing with other ''terra incognita'' problems.

SIGNIFICANCE STATEMENT: Turbulent motions are produced through instability development. Advection schemes designed to avoid generating spurious oscillations in flow fields involving sharp gradients may also suppress the development of physically realistic instabilities. This work explores the influence of advection schemes on numerical simulations that resolve turbulent motions. Recommendations are made concerning the use of advection schemes in simulating atmospheric turbulence, which is almost always accompanied with thermodynamic processes involving sharp temperature and moisture gradients. In addition, an advection-scheme-based concept is proposed to reproduce turbulent motions that are inadequately resolved by simulation grids.

KEYWORDS: Turbulence; Boundary layer; Surface layer; Large eddy simulations

1. Introduction

Weighted essentially nonoscillatory (WENO) advection schemes are widely used in computational fluid dynamics (CFD), in both finite-difference and finite-volume codes, to handle gradients that are too sharp to be resolved by the given numerical grids (Shu 2003). Specifically, WENO schemes reduce the spurious oscillations caused by using values at three or more grid points to compute high-order approximations of fluxes of a variable when discontinuities or sharp gradients are present (Jiang and Shu 1996; Henrick et al. 2005; Borges et al. 2008). Examples of WENO applications include simulations involving sharp gradients of momentum [e.g., supersonic jet and free shear layer (Cheng and Lee 2005)] and sharp gradients of scalars [e.g., thermal bubbles, density currents (Pressel et al. 2015), and clouds (Pressel et al. 2017)]. The thermodynamic processes in the atmosphere often involve sharp temperature and moisture gradients, and therefore WENO schemes are among the available advection schemes in popular atmospheric models like the Weather Research and Forecasting (WRF; Skamarock and Klemp 2008) Model and Cloud Model 1 (CM1; Bryan and Fritsch 2002).

When WENO schemes are used to reduce spurious oscillations generated by the numerical treatment of advection, they also damp the physically realistic oscillations associated with instability development. Shear instability, which naturally amplifies oscillations (Drazin and Reid 2004), is vital to the cascade of energy from large to small scales. As a result, WENO schemes that damp oscillations indiscriminately may suppress the energy cascade in turbulence-resolving simulations [i.e., direct numerical simulation (DNS) and large-eddy simulation (LES)] and subsequently lead to unsatisfactory predictions of turbulence characteristics. Lunet et al. (2017) have shown evidence of LES results of resolved turbulence being damped by WENO schemes. The numerical modeling of moist convection processes in the atmosphere requires using LES to reveal the time-evolving aspect of the turbulent atmospheric boundary layer (ABL) and cloud dynamics (Bryan and Fritsch 2002; Bryan et al. 2003), while WENO schemes are usually also employed to handle the sharp temperature and moisture gradients at cloud edges (Pressel et al. 2017). Given the common use of WENO schemes in meteorological LES, a comprehensive investigation of the influence of WENO schemes on resolved turbulent motions in LES is warranted.

Corresponding author: Aaron Wang, auw317@psu.edu

DOI: 10.1175/JAS-D-21-0033.1

TABLE 1. A total of 12 runs conducted to explore the influence of WENO schemes on CM1 LES results of a quasi-steady, horizontally homogeneous, fully developed, neutral ABL.

Case	WENO schemes applied to momentum/scalar	Δx, Δy (m)	Δz (m)
MSWENO-DX25DZ25	Yes/yes	25	25
MWENO-DX25DZ25	Yes/no	25	25
SWENO-DX25DZ25	No/yes	25	25
NOWENO-DX25DZ25	No/no	25	25
MSWENO-DX10DZ10	Yes/yes	10	10
MWENO-DX10DZ10	Yes/no	10	10
SWENO-DX10DZ10	No/yes	10	10
NOWENO-DX10DZ10	No/no	10	10
MSWENO-DX25DZ10	Yes/yes	25	10
MWENO-DX25DZ10	Yes/no	25	10
SWENO-DX25DZ10	No/yes	25	10
NOWENO-DX25DZ10	No/no	25	10

This work focuses on the influence of WENO schemes on turbulence within the atmospheric surface layer, where turbulent motions are actively produced through instability development (see Stull 1988, Fig. 5.4). Theoretically, the mean-wind profile in a statistically steady, horizontally homogeneous, fully developed, neutral surface layer (hereafter referred to as an "idealized surface layer") follows the law of the wall (LOTW; Prandtl 1933), providing an a priori test of any LES code. In this work, the influence of WENO schemes on resolved turbulent motions in an idealized surface layer is investigated using the CM1 LES code. CM1 is a versatile atmospheric model that has been used to simulate various moist convection processes (e.g., Bryan and Fritsch 2002; Bryan et al. 2003; Tushaus et al. 2015; Shi et al. 2018).

The rest of the paper is arranged as follows. Section 2 describes methodology, including how WENO schemes are applied to CM1, the configuration of CM1 LES runs, and the filtered LOTW needed for evaluating LES results. Section 3 presents the results of the effects of WENO schemes on acoustic waves, surface-layer turbulence, and energy cascade, as well as the sensitivity of WENO-scheme effects to grid spacing. Inspired by the influence of WENO schemes on energy cascade, section 4 proposes a concept of anti-WENO (AWENO) schemes to improve the prediction of energy cascade when energy-containing turbulent motions are inadequately resolved by LES grids. The conclusions are presented in section 5. Appendixes provide detailed formulation of the fifth-order advection scheme and the corresponding WENO scheme (which are available in CM1), as well as the newly proposed AWENO schemes.

2. Methodology

a. *CM1 LES governing equations and available WENO options*

This work simulates a dry ABL using CM1 (version 19.10), which is a compressible, nonhydrostatic, three-dimensional atmospheric model (Bryan and Fritsch 2002; Bryan 2017). The code solves prognostic equations for the three velocity components (u, v, w), potential temperature perturbation from its initial state [θ'', where the double prime ($''$) represents the perturbation of a variable from its initial state], nondimensional pressure perturbation from its initial state [π'', where $\pi = (p/p_{00})^{R/c_p} = T/\theta$, T is temperature, θ is potential temperature, p is pressure, p_{00} is a reference pressure (=1000 hPa), R is the gas constant for dry air, and c_p is the specific heat of dry air at constant pressure]. Moist processes are turned off in the simulations.

The LES closure employs a turbulent kinetic energy (TKE) subgrid-scale (SGS) model (Deardorff 1980), which solves an additional prognostic equation of SGS TKE (e). The relationship between the SGS stress tensor and the resolved velocity gradient tensor is characterized by a scalar eddy viscosity,

$$K_m = 0.10le^{1/2}, \tag{1}$$

which is composed of a velocity scale given by the square root of the SGS TKE ($e^{1/2}$) and a length scale (l) given by a combination of the grid spacing (Δ), the distance from the surface (z), and the stratification. For neutral and unstable conditions (Mason and Thomson 1992),

$$\frac{1}{l^2} = \frac{1}{\Delta^2} + \frac{1}{[\kappa(z + z_0)]^2}, \tag{2}$$

where $\Delta = (\Delta x \Delta y \Delta z)^{1/3}$, Δx, Δy, and Δz are streamwise, spanwise, and vertical grid spacings, respectively, $\kappa = 0.4$ is the von Kármán constant, and z_0 is the roughness length. The length scale (l) given by (2) decreases with decreasing z (i.e., as one approaches the surface). For stable conditions, a length scale (l_{stb}) inversely proportional to the Brunt–Väisälä frequency is computed (Deardorff 1980), and l is given by the minimum of l_{stb} and (2).

The advection operators in CM1 employ the finite-volume method and typically use values at three or more grid points to compute spatial derivatives with a high order of accuracy. When the field of interest contains a discontinuity or a sharp gradient, using a high-order finite-volume scheme often leads to spurious oscillations. WENO schemes are capable of

TABLE 2. As in Table 1, but for the four additional runs conducted to explore the influence of the newly proposed AWENO schemes. For each of the runs WENO schemes are applied to scalar advection whereas AWENO schemes are applied to momentum advection.

Case	AWENO schemes applied to momentum advection at	q (–)	Δx, Δy (m)	Δz (m)
AWENO-q0.5-DX25DZ25	$z \le 4\Delta z$	0.5	25	25
AWENO-q2-DX25DZ25	$z \le 4\Delta z$	2	25	25
AWENO-q0.5-DX25DZ10	$z \le 6\Delta z$	0.5	25	10
AWENO-q2-DX25DZ10	$z \le 6\Delta z$	2	25	10

reducing spurious oscillations by targeting discontinuous locations suggested by large values of first- and second-order spatial derivatives. When small-scale oscillations are smoothed by WENO schemes, numerical diffusion[1] occurs in the physical space (Borges et al. 2008). Appendix A provides the details of the widely used fifth-order advection scheme and the corresponding WENO scheme, which are used in this work.

WENO schemes can be applied to both scalar[2] (θ'', e) and momentum (u, v, w) fields. The default CM1 namelist options (version 19.10) recommend applying WENO schemes to scalar fields but not to momentum fields for the sake of optimizing computational performance. Specifically, without using WENO schemes, a sufficiently fine resolution is needed to resolve sharp gradients and therefore to avoid generating spurious oscillations. Applying WENO schemes to scalar fields enables the use of relatively coarse resolution without generating spurious oscillations, and therefore reduces computational cost (Pressel et al. 2015). However, applying WENO schemes to the momentum field does not yield any apparent further reduction in computational cost (G. Bryan 2020, personal communication).

b. Configuration of CM1 LES runs

The CM1 LES runs are configured to simulate a quasi-steady, horizontally homogeneous, fully developed, neutral ABL flow in an inertial frame of reference. The domain is 10 km × 10 km × 4 km with periodic lateral boundary conditions. The upper boundary is rigid and free-slip. Rayleigh damping is applied to the momentum field above a height of 2.4 km to reduce the reflection of waves from the upper boundary. The lower boundary condition follows LOTW (one of the "semislip" surface-model options in CM1) with a roughness length of $z_0 = 0.12$ m. Each LES run starts from a neutrally stratified ABL capped by an inversion at $z = 1$ km. The initial velocity field is uniform, with $\tilde{u} = 10$ m s^{-1} and $\tilde{v} = \tilde{w} = 0$ everywhere. Here the tildes represent filtering over the LES's grid spacing. Random perturbations with an amplitude of 0.25 K are imposed on the initial potential temperature field to trigger turbulence. The mean horizontal pressure gradient is zero, so that the flow is driven by inertia. Note that an inertia-driven ABL yields slowly decaying turbulent flow, which may not be ideal to be evaluated against LOTW derived for a true statistically steady-state condition. Nevertheless, nonstationarity at scales much larger than the large-eddy turnover time is expected to have little influence on the applicability of LOTW to a neutral atmospheric surface layer (Wyngaard 2010). Thus, an inertia-driven ABL is good enough for the current work, whose objective is to understand the influence of WENO schemes on the simulated turbulence. An additional reason of simulating an inertia-driven ABL is to keep a simulation configuration as similar as possible to the "LES-TURB" run conducted by Markowski and Bryan (2016), so that the current work does not need to repeat some of the previously published analysis results.

Table 1 summarizes a total of 12 simulations conducted to study the influence of WENO schemes on the simulated turbulence. The first set of simulations is conducted using a grid spacing of $\Delta x = \Delta y = \Delta z = 25$ m to study the influence of the WENO schemes: 1) WENO schemes applied to both scalar and momentum fields (MSWENO-DX25DZ25), 2) WENO schemes applied to momentum field only (MWENO-DX25DZ25), 3)

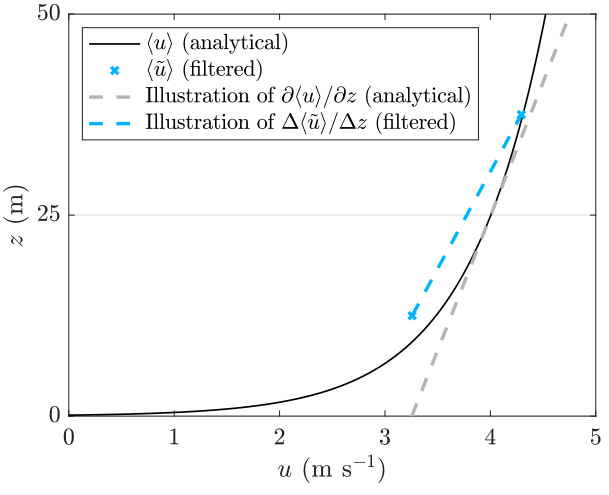

FIG. 1. The difference in shear at $z = \Delta z = 25$ m given by the analytical (gray dashed line) and filtered LOTW (cyan dashed line). The black solid line represents the theoretical logarithmic wind profile, and the cyan crosses represent the values obtained by filtering the black line over each Δz.

[1] The numerical diffusion of WENO schemes is called *dissipation* in some studies (Borges et al. 2008; Pressel et al. 2017). Diffusion is more accurate than dissipation because the smoothed quantities are spatially redistributed rather than removed from the system of interest (see Fig. 4 in Borges et al. 2008).

[2] In CM1, the scalar field that WENO schemes applied to does not include the pressure field.

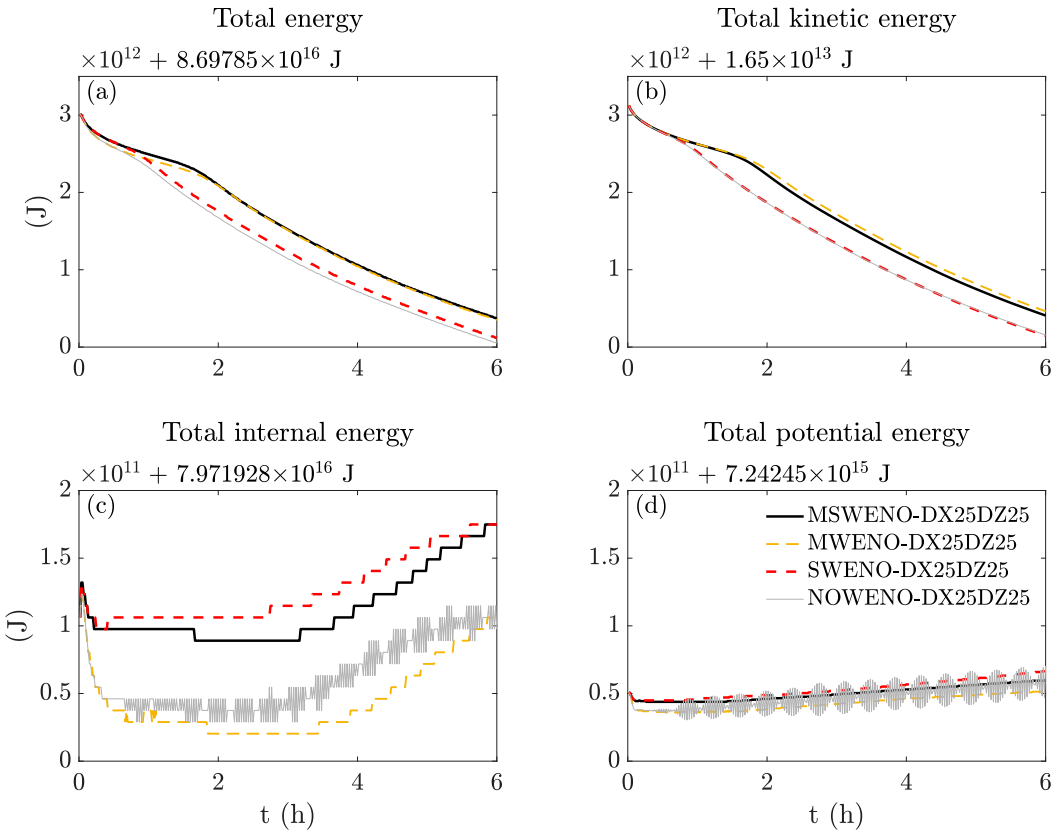

FIG. 2. Time series of the (a) total energy, (b) total kinetic energy, (c) total inertial energy, and (d) total potential energy. The four simulations shown in each panel are conducted using a $(25\,\text{m})^3$ grid spacing. The steplike patterns in total internal energy in (c) are because CM1 stores the statistics with limited precision. Specifically, variables shown here are diagnostic statistic output from CM1, where each uses up to seven significant digits. The total internal energy is on the order of 10^{16} J, meaning that its minimum variation (10^{10} J) is only an order of magnitude smaller than the *y*-axis range shown in (c) (10^{11} J), and therefore it appears as steplike nonsmooth patterns. The other panels do not show steplike patterns because the minimum variation of the associated variable is at least two orders of magnitude smaller than the corresponding *y*-axis range. The "wave groups" NOWENO results in (c) and (d) are induced by taking output every 1 min, which is less frequent than the oscillations of domain-total vertical velocity shown in Fig. 3 (every 24 s).

WENO schemes applied to scalar field only (SWENO-DX25DZ25), and 4) WENO schemes not applied to any field (NOWENO-DX25DZ25). When WENO schemes are not applied, fifth-order advection schemes are applied instead (appendix A). Each case name is composed of the use of WENO schemes and the grid spacing. MSWENO-DX25DZ25 is configured the same as the "LES_TURB" simulation in Markowski and Bryan (2016), except for using a newer version of CM1. Because advection in numerical simulation is sensitive to grid spacing (Bott 1989; Tremback et al. 1987), two similar sets of simulations are conducted using alternative grid spacings [$\Delta x = \Delta y = \Delta z = 10$ m (-DX10DZ10) and $\Delta x = \Delta y = 25$ m, $\Delta z = 10$ m (-DX25DZ10)] to investigate the influence of grid spacing on advection handled by WENO schemes. In addition to the 12 simulations in Table 1, four simulations are conducted using the newly proposed AWENO schemes (summarized in Table 2) to explore the potential of reproducing underresolved turbulent motions by modulating advection schemes (see details in section 4 and appendix B).

Each of the simulations shown in Tables 1 and 2 runs for 6 h with a time step of 0.4 s. LES results of ABL turbulence have reached quasi-steady state after $t = 3$ h (see details in section 3b). CM1 uses a third-order Runge–Kutta method for the time integration. The WENO schemes, if applied, are computed on the final Runge–Kutta step.[3] Using a fixed time step and the same domain and grid spacing configuration, applying WENO schemes has negligible effect on the computational cost (within ±8% and not systematic).

[3] Applying WENO schemes at every Runge–Kutta step shows little advantage compared to applying at only the final step (G. Bryan 2021, personal communication). Thus, WENO schemes are applied to only the final Runge–Kutta step to optimize computational performance.

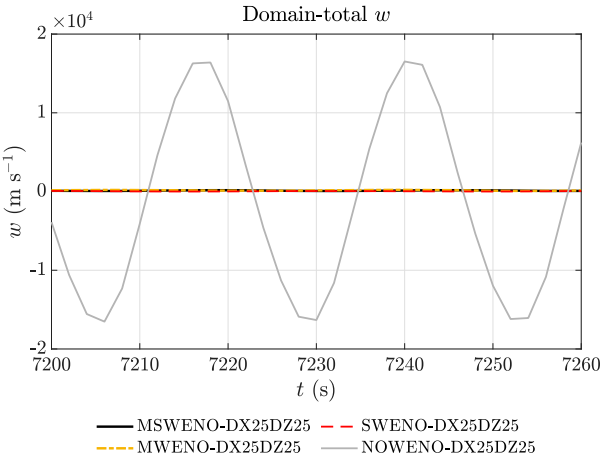

FIG. 3. Time series of the domain-total vertical velocity from four simulations conducted using a $(25\,\mathrm{m})^3$ grid spacing. The output frequency is every 2 s.

c. *Filtering LOTW for the purpose of evaluating LES results*

LOTW is the theoretical prediction of the stress–strain-rate relationship within a statistically steady-state, horizontally homogeneous, fully developed, neutral surface layer (Prandtl 1933), where the nondimensional vertical wind shear is given by

$$\phi_m = \frac{\kappa z}{u_*}\frac{\partial \langle u\rangle}{\partial z} = 1. \tag{3}$$

Here u_* is the friction velocity, $\langle u\rangle$ is the Reynolds average of streamwise velocity (indicated by angled brackets, and is approximated using the horizontal average in this work), z is the height above the surface, and $\kappa = 0.4$ is the von Kármán constant.

To evaluate the LES results of the spatially filtered velocity field, LOTW needs to be filtered over the LES's vertical grid spacing. Filtering $\langle u\rangle$ over the LES's grid spacing yields

$$\widetilde{\langle u(z)\rangle} = \frac{1}{\Delta z}\int_{z-\Delta z/2}^{z+\Delta z/2} \langle u(z')\rangle\, dz'. \tag{4}$$

Because both spatial filtering and horizontal averaging are linear operators, $\widetilde{\langle u(z)\rangle} = \langle \tilde{u}(z)\rangle$, meaning that $\widetilde{\langle u(z)\rangle}$ given by (4) can be used to evaluate horizontally averaged LES results of filtered velocity $[\langle \tilde{u}(z)\rangle]$. Figure 1 shows that the differences between $\langle \tilde{u}(z)\rangle = \widetilde{\langle u(z)\rangle}$ and $\langle u(z)\rangle$ are most profound near the surface, where the $\langle u\rangle$ profile is highly nonlinear. Specifically, filtering over the first grid ($0 \le z \le \Delta z$) yields

$$\begin{aligned}\left\langle \widetilde{u\left(\frac{\Delta z}{2}\right)}\right\rangle &= \frac{1}{\Delta z}\int_{z_0}^{\Delta z}\frac{u_*}{\kappa}\ln\left(\frac{z'}{z_0}\right)dz' \\ &= \frac{u_*}{\kappa\Delta z}\int_{z_0}^{\Delta z}[\ln(z') - \ln(z_0)]\,dz' \\ &= \frac{u_*}{\kappa\Delta z}\{z'[\ln(z') - 1] - z'\ln(z_0)\}\Big|_{z_0}^{\Delta z} \\ &= \frac{u_*}{\kappa}\left[\ln\left(\frac{\Delta z}{z_0}\right) - 1 + \frac{z_0}{\Delta z}\right],\end{aligned} \tag{5}$$

which differs from

$$\left\langle u\left(\frac{\Delta z}{2}\right)\right\rangle = \frac{u_*}{\kappa}\ln\left(\frac{\Delta z}{2z_0}\right). \tag{6}$$

For $\Delta z = 25$ m and $z_0 = 0.12$ m, $\langle \tilde{u}\rangle$ is 6.5% smaller than $\langle u\rangle$ at $z = \Delta z/2$, and correspondingly the filtered nondimensional shear,

$$\tilde{\phi}_m = \frac{\kappa z}{u_*}\frac{\partial \langle \tilde{u}\rangle}{\partial z}, \tag{7}$$

is 38% larger than $\phi_m = 1$ at $z = \Delta z$ (which is the second W level[4]) with the vertical gradient calculated by a second-order centered difference. LES results of nondimensional shear should be evaluated against the theoretical $\tilde{\phi}_m$ (i.e., filtered LOTW) rather than ϕ_m, or otherwise the resulting excessive overshoot in near-surface nondimensional shear is potentially misleading. In other words, the discrepancy between LES results and the theoretical $\tilde{\phi}_m$ provides a measure of the log-layer mismatch, whereas the discrepancy between the theoretical $\tilde{\phi}_m$ and $\phi_m = 1$ is not a true log-layer mismatch.

3. Results

a. *The advantage of using WENO schemes*

Figure 2 shows the time series of total energy, kinetic energy, internal energy, and potential energy over the entire domain given by simulations using a $(25\,\mathrm{m})^3$ grid spacing (the first four runs in Table 1). The dissipation of kinetic energy [$\sim O(10^{12})$ J] of an inertia-driven ABL flow leads to a decrease of total energy with time (Fig. 2a). Simulations with WENO schemes applied to momentum advection (MSWENO-DX25DZ25 and MWENO-DX25DZ25) show a slower decrease of the kinetic energy and thus the total energy (Figs. 2a,b) than simulations without WENO schemes applied to momentum advection (SWENO-DX25DZ25 and NOWENO-DX25DZ25). The relatively slow decrease of kinetic energy suggests relatively slow energy dissipation rate.

The advantage of using WENO schemes is evident in the time series of internal and potential energy (Figs. 2c,d). Without WENO schemes (NOWENO-DX25DZ25), the internal and potential energy over the entire domain oscillate in time (see the gray solid lines in Figs. 2c,d). Focusing on a 24-s period starting at $t = 2$ h, a complete cycle of the oscillation is evident in the domain-total vertical velocity component (Fig. 3). The domain-total vertical velocity is associated with the propagation of acoustic waves in the vertical direction, demonstrated by the periodic variation of pressure perturbations (p'' in Figs. 4a–g), whose 24-s period matches the time taken by acoustic waves (characterized by a

[4] Because CM1 uses a C grid, we use U level and W level interchangeably in the context. U level is the level where the horizontal velocities vertically located (including U grid for streamwise velocity, V grid for spanwise velocity, and Θ grid for scalar field, while these three grids are horizontally different), and W level is the level of W grid (for vertical velocity and SGS-TKE). The first U level is at $z = \Delta z/2$, and the first W level is at $z = 0$.

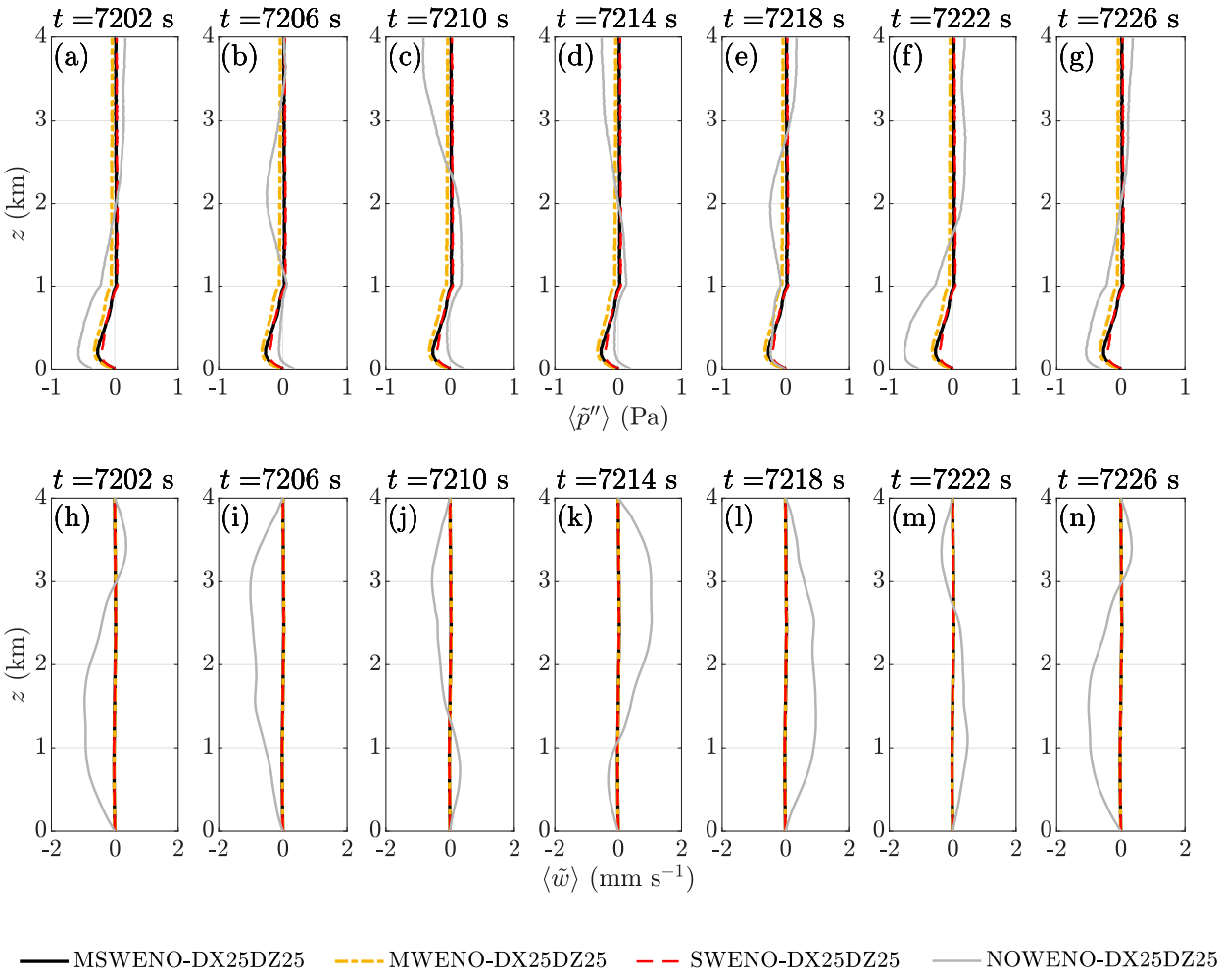

FIG. 4. The horizontally averaged (a)–(g) pressure perturbation from initial state and (h)–(n) vertical velocity from the four simulations conducted using a $(25\,\mathrm{m})^3$ grid spacing. The time increment between adjacent columns is 4 s.

phase speed of approximately $340\,\mathrm{m\,s^{-1}}$) to complete a round trip across the 4-km vertical domain. When the acoustic waves reach the top (bottom) boundaries, the accumulated pressure perturbations induce an upward (downward) pressure gradient force in the vertical direction, which then leads to nonzero domain-total vertical velocity. Figures 4f, 4g, 4m, and 4n show the formation of downward pressure gradient force followed by the development of downward vertical velocity. The propagation of acoustic waves are too fast for the Rayleigh damping applied above 2.4 km of the domain to damp the associated vertical velocity oscillation effectively. Applying WENO schemes to either the momentum or scalar fields can eliminate the propagation of acoustic waves, which ensures that the horizontally averaged vertical velocities remains nearly zero at all heights (see the black solid, yellow dotted–dashed, and red dashed lines in Fig. 4).

b. *The influence of WENO schemes on surface-layer turbulence*

The decrease of total energy with time (Fig. 2a) leads to the decrease of both kinetic energy (Fig. 2b) and friction velocity (not shown) with time. Nevertheless, the components of resolved stress tensor scaled by the square of friction velocity become approximately constant with time after $t = 3$ h. Thus, LES results of ABL turbulent motions have reached a quasi-steady state after $t = 3$ h, whose surface-layer statistics can be evaluated against the filtered LOTW. As aforementioned in section 2c, the discrepancy between quasi-steady-state LES results of filtered nondimensional shear ($\tilde{\phi}_m$) and the filtered LOTW (e.g., the cyan dotted line Fig. 5a) provides a measure of the log-layer mismatch. Figure 5a shows that simulations applying WENO schemes to momentum advection (MSWENO and MWENO) yield larger log-layer mismatch than simulations without applying WENO schemes to momentum advection (SWENO and NOWENO).

The log-layer mismatch is linked to insufficiently resolved momentum flux near the surface. In a quasi-steady, horizontally homogeneous, fully developed, neutral ABL, the magnitude of the total momentum flux decreases linearly with height (e.g., see Fig. 3 in Markowski and Bryan 2016). When resolved turbulent motions do not carry sufficient amount of momentum flux, the SGS model is forced to make up whatever

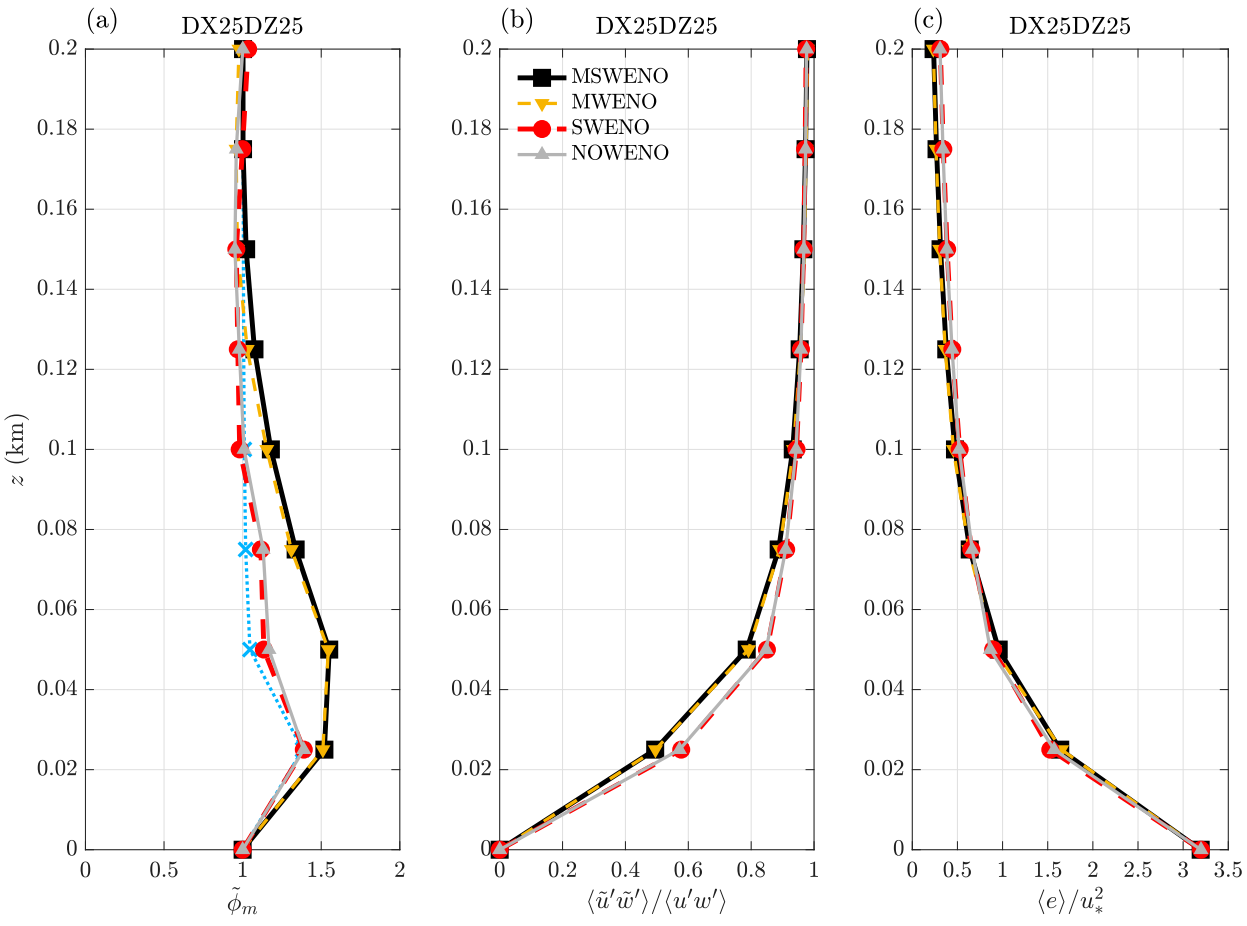

FIG. 5. Profiles of (a) the quasi-steady-state nondimensional shear, (b) the ratio of resolved to total shear stress, and (c) the scaled SGS TKE from the four simulations conducted using a $(25\,\mathrm{m})^3$ grid spacing. LES results are averaged over the horizontal domain and $5 \le t \le 6$ h. The nondimensional shear results are evaluated against LOTW filtered with $\Delta z = 25$ m [cyan dotted line in (a)].

remaining fraction of the total momentum flux. Given an eddy-viscosity type of SGS model, increasing the SGS momentum flux requires increasing either the resolved velocity gradients or the eddy viscosity, or both. For the TKE-SGS model, the eddy viscosity given by (1) is composed of a length scale (l) and a velocity scale ($e^{1/2}$). For neutral conditions, the length scale (l) given by (2) at a given height (z) is fixed for a given grid spacing (Δ), meaning that the only possible way to increase the eddy viscosity is via increasing the SGS TKE. Increasing the shear production of SGS TKE then requires increasing the resolved velocity gradients. In short, when resolved motions fail to produce sufficient momentum flux, the TKE SGS model demands unrealistically large resolved velocity gradients to make up any needed momentum flux. Thus, the CM1 LES employing the TKE SGS model overestimates the near-surface nondimensional shear, and the overestimation is amplified when the resolved momentum flux is further reduced by applying the WENO schemes to momentum advection. Specifically, applying WENO schemes to momentum advection decreases the ratio of resolved to total momentum fluxes ($\langle \tilde{u}'\tilde{w}' \rangle / \langle u'w' \rangle$ shown in Fig. 5b, where $\langle u'w' \rangle$ is the sum of the resolved and SGS fluxes) and amplifies log-layer mismatch (Fig. 5a). WENO schemes also damps the production of SGS TKE, but the resulting over-predicted mean shear near the surface yields slightly higher SGS TKE (for $z < 0.07$ km in Fig. 5c). Nevertheless, the change in SGS TKE is minor compared to the change in resolved momentum stress and nondimensional shear. LES results obtained using the Smagorinsky and dynamic SGS models also show that the overestimation of the near-surface nondimensional shear is linked to insufficient momentum flux produced by resolved motions (Mason and Thomson 1992; Porté-Agel et al. 2000; Bou-Zeid et al. 2005; Brasseur and Wei 2010).

The amplification of log-layer mismatch induced by applying WENO schemes to momentum advection is robust across all LES grid spacings tested in this work (Figs. 5–7). For a grid aspect ratio $\Delta x/\Delta z = 1$, the peak enhancement of log-layer mismatch induced by applying WENO schemes to momentum advection is always at the third W level with a difference of about 0.5 in $\tilde{\phi}_m$ (comparing MSWENO and MWENO results to SWENO and NOWENO results in Figs. 5a and 6a). For $\Delta z = 10$ m, increasing the horizontal grid spacing (Δx) from 10 to 25 m reduces the ratio of resolved to total momentum fluxes at the lowest 10 or more W levels (comparing Figs. 6b and 7b). With a grid aspect ratio of $\Delta x/\Delta z = 2.5$, the peak enhancement of

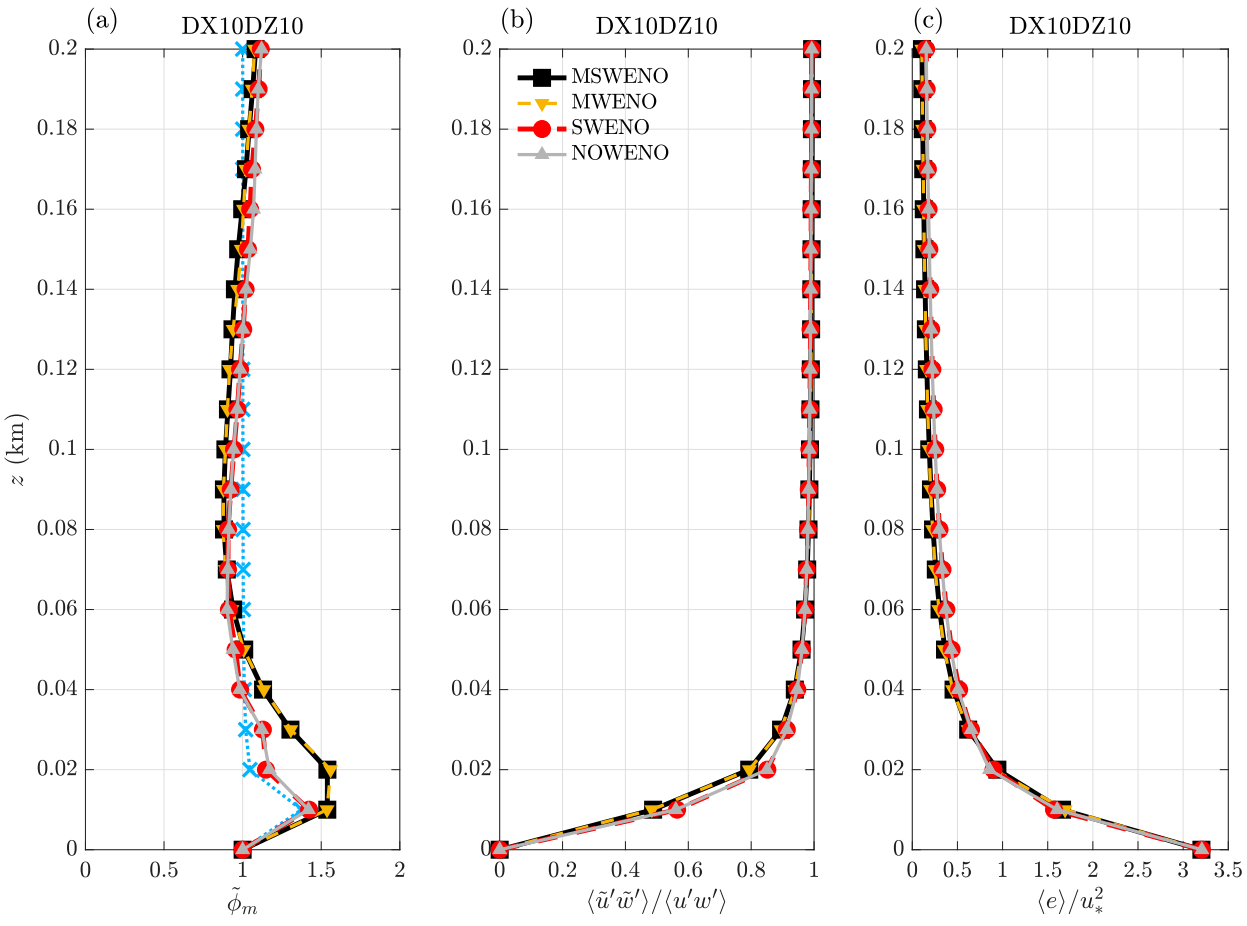

FIG. 6. As in Fig. 5, except that results are from the four simulations using a $(10\,\text{m})^3$ grid spacing, and the LOTW is filtered with $\Delta z = 10$ m.

log-layer mismatch induced by applying WENO schemes to momentum advection is located at the fourth W level with a difference of about 0.8 in $\tilde{\phi}_m$ (comparing MSWENO and MWENO results to SWENO and NOWENO results in Fig. 7a). The increase of log-layer mismatch with increasing $\Delta x/\Delta z$ [investigated by previous studies like Brasseur and Wei (2010)] is further amplified by applying WENO schemes to momentum advection.

c. *The role of WENO schemes in amplifying the log-layer mismatch by suppressing the energy cascade*

The results in section 3b show that applying WENO schemes to scalar advection has negligible impacts on surface-layer statistics (comparing MSWENO results to MWENO results or comparing SWENO results to NOWENO results in Figs. 5–7). Results in section 3a show that the simulation without applying WENO schemes (i.e., NOWENO) suffers from the reflection of acoustic waves at the top boundary. This subsection focuses on the comparison between MSWENO and SWENO results to explore the influence of applying WENO schemes to momentum advection on ABL turbulence.

As aforementioned in the introduction, WENO schemes are expected to suppress instability development in LES, which is essential for the production of resolved turbulent motions. Figure 8 shows structures of resolved turbulence at $t = 6$ h visualized by the λ_2 method proposed by Jeong and Hussain (1995). Here λ_2 is the second eigenvalue of $\mathbf{S}\cdot\mathbf{S} + \mathbf{\Omega}\cdot\mathbf{\Omega}$, where $\mathbf{S}$ and $\mathbf{\Omega}$ are the symmetric and antisymmetric parts of the resolved velocity gradient tensor $(\nabla\tilde{u})$. Comparing Figs. 8a and 8c to Figs. 8b and 8d shows that applying WENO schemes to momentum advection damps resolved turbulence structures in the entire ABL.

The role of WENO schemes in suppressing instability development is also evident in the reduction of turbulent vortex stretching, $||\tilde{\boldsymbol{\omega}}' \cdot \nabla\tilde{u}'||$ (see Davidson 2015, chapter 4.4.1), especially near the surface (comparing MSWENO and SWENO results in Fig. 9). Here $\tilde{\boldsymbol{\omega}}' = \nabla \times \tilde{u}'$ is the resolved vorticity vector perturbation and $\|\tilde{\boldsymbol{\omega}}' \cdot \nabla\tilde{u}'\|$ represents the magnitude (i.e., square norm) of the dot product between $\tilde{\boldsymbol{\omega}}'$ and $\nabla\tilde{u}'$. The turbulent vortex stretching drives energy cascade from large to small scales (Tennekes and Lumley 1972; Davidson 2015). Thus, applying WENO schemes to momentum advection is expected to suppress energy cascade. Direct evidence is provided by the MSWENO results of near-surface streamwise energy spectrum, which shows accumulated energy at large scales ($kz < 0.1$) and lack of energy at small scales ($kz > 0.2$) (comparing the black and red solid lines in Fig. 10). In shear-dominated flows, TKE production occurs in the streamwise

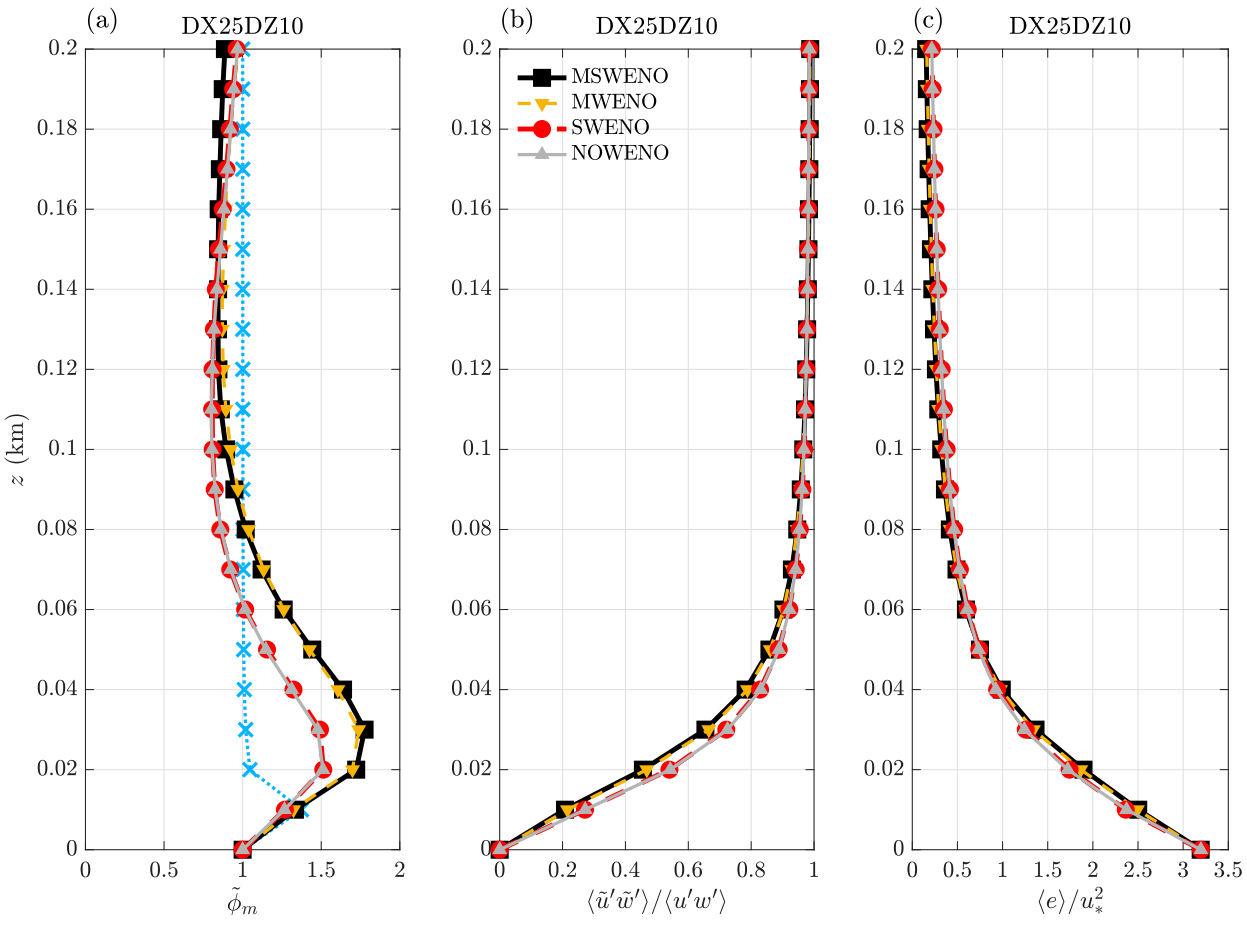

FIG. 7. As in Fig. 6, except that the results are from the four simulations using a 25 m × 25 m × 10 m grid spacing.

direction and then TKE is transferred to the other two directions through the interaction with pressure perturbations (Tennekes and Lumley 1972; Pope 2000). The pressure–velocity interaction is associated with the resolved linear strain rates ($\partial\tilde{u}/\partial x$, $\partial\tilde{v}/\partial y$, $\partial\tilde{w}/\partial z$; see Tennekes and Lumley 1972, chapter 3.2), which become increasingly profound with decreasing scale of motion. Thus, the suppressed energy cascade from large to small scales in the streamwise direction leads to a reduced vertical energy spectrum at all scales (comparing the black and red dashed lines in Fig. 10). Similar effects of WENO schemes on energy spectra are reported by (Lunet et al. 2017).

The suppressed energy cascade is also revealed by MSWENO results of relatively large resolved streamwise velocity variance ($\langle \tilde{u}'\tilde{u}' \rangle$) and relatively small velocity variance in the other two directions ($\langle \tilde{v}'\tilde{v} \rangle$ and $\langle \tilde{w}'\tilde{w}' \rangle$), as shown in Fig. 11a. The relatively small $\langle \tilde{w}'\tilde{w}' \rangle$ leads to a relatively small shear production of $\langle \tilde{u}'\tilde{w}' \rangle$ (comparing the red line and the black line in Fig. 11b), which is given by

$$\tilde{P}_{13} = -\langle \tilde{w}'\tilde{w}' \rangle \frac{\partial \langle \tilde{u} \rangle}{\partial z} \tag{8}$$

for the current flow of interest (i.e., $\langle \tilde{w} \rangle = 0$ and $\partial\langle \tilde{u} \rangle/\partial x = \partial\langle \tilde{u} \rangle/\partial y = 0$). Thus, applying WENO schemes to momentum advection reduces the shear production of $\langle \tilde{u}'\tilde{w}' \rangle$, which eventually reduces $\langle \tilde{u}'\tilde{w}' \rangle$ and amplifies log-layer mismatch.

4. Anti-WENO: A means of enhancing the energy cascade and reproducing LOTW

Previous studies have also reported the connection between log-layer mismatch and the streamwise energy spectrum (e.g., Porté-Agel et al. 2000; Bou-Zeid et al. 2005), similar to the findings in section 3c. Unlike the current work focusing on advection schemes, previous studies have investigated the role of SGS models. For example, compared to the standard Smagorinsky SGS model, the Lagrangian scale-dependent dynamic Smagorinsky model dissipates less energy near the surface and dissipates more energy aloft (combining Figs. 1 and 2b in Bou-Zeid et al. 2005). Consequently, the Lagrangian scale-dependent dynamic Smagorinsky model yields a near-surface streamwise energy spectrum containing less energy at large scales ($kz < 0.02$) and more energy at small scales ($kz > 0.04$) compared to the standard Smagorinsky model (comparing the top curve in Fig. 3d to the top curve in Fig. 3a in Bou-Zeid et al. 2005). A near-surface streamwise energy spectrum with reduced energy at large scales and enhanced energy at small scales increases the contribution of resolved momentum

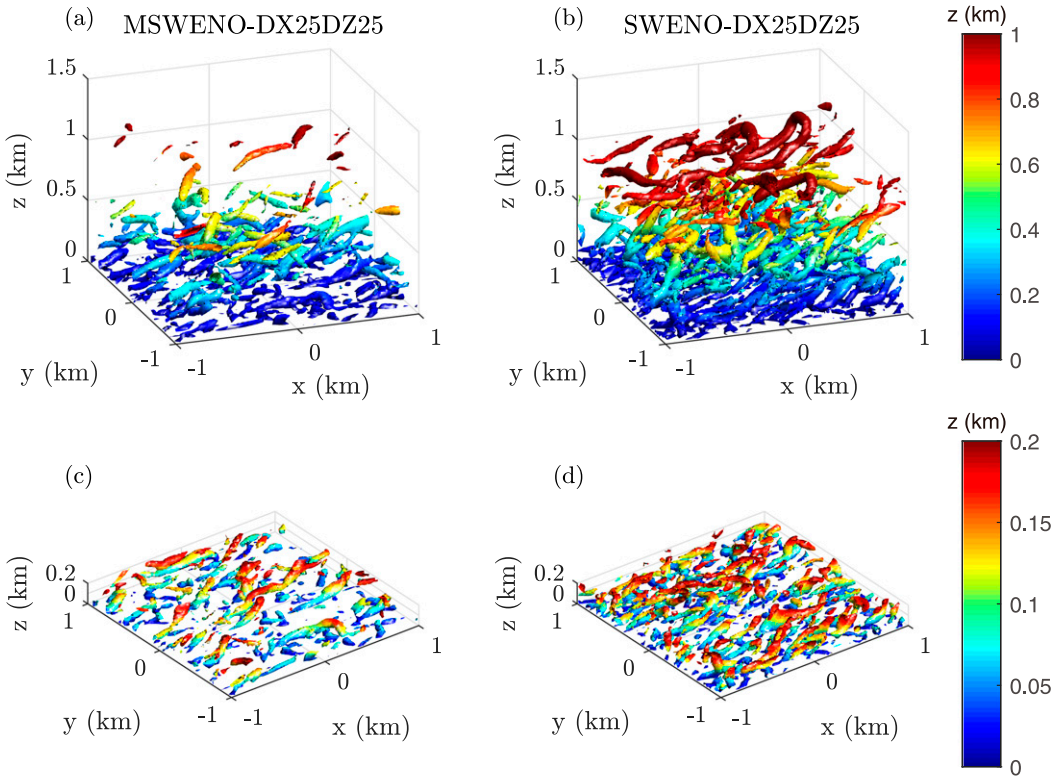

FIG. 8. Resolved turbulence structures at $t = 6$ h in (a),(b) the ABL and (c),(d) particularly the surface layer from (a),(c) MSWENO-DX25DZ25 and (b),(d) SWENO-DX25DZ25 simulations. The structures are visualized by the isosurface, which represents $\lambda_2 = -1 \times 10^{-4}\,\mathrm{s}^{-2}$. Physically, $\lambda_2 < 0$ implies the existence of a vortex core, and λ_2 represents the vortical-contributed local pressure minimum [see section 4 in Jeong and Hussain (1995)]. The colors show the vertical location of the isosurface.

flux to the total momentum flux (see Fig. 4 in Bou-Zeid et al. 2005) and reduces the magnitude of nondimensional shear (Fig. 2b in Bou-Zeid et al. 2005), consistent with the current findings based upon modifying advection schemes. These results suggest that reproducing LOTW requires appropriate distribution of energy across scales, but it does not distinguish whether the energy spectrum is produced by modulating SGS models or advection schemes. Bou-Zeid et al. (2005) have shown success in reproducing LOTW using the Lagrangian scale-dependent dynamic Smagorinsky model. In this section, we will show that LOTW can also be reproduced by modifying advection schemes.

The role of WENO schemes in suppressing instability development and energy cascade inspires a concept of AWENO schemes to enhance instability development and energy cascade. Technically, the smoothness indicator computed by WENO schemes is used to *amplify* rather than reduce oscillations (see appendix B). In this work, AWENO schemes are applied to only momentum advection near the surface, where roughly 10% or more of the total momentum flux is unresolved. Specifically, AWENO schemes are applied to momentum advection at $z \le 4\Delta z$ for simulations using a grid spacing of DX25DZ25 and at $z \le 6\Delta z$ for simulations using a grid spacing of DX25DZ10 (see details in Table 2). Figure 9 shows that applying AWENO schemes to momentum advection increases the local turbulent vortex stretching [see the green and blue lines for $z < 100$ m (i.e., $4dz$, where $dz = 25$ m)]. The increased turbulent vortex stretching is consistent with enhanced energy cascade revealed by the streamwise energy spectrum, which shows reduced energy at relatively large scales and increased energy at relatively small scales (comparing the green, blue, and red solid lines in Figs. 10 and 12). The effectiveness of AWENO schemes in amplifying instability development increases with increasing q, which controls the sensitivity of WENO and AWENO schemes to sharp velocity gradients [see (A10) and (B1) in appendixes A and B].

The choice of q value is bounded by physical expectations of the energy spectra. As aforementioned in section 3c, TKE production in shear-dominated flows occurs in the streamwise direction and then transfers to the other two directions. Thus, the surface-layer streamwise energy spectrum is expected to be larger than energy spectra in the other two directions across all scales. Using a grid spacing of DX25DZ25, applying AWENO schemes with $q = 2$ yields a vertical energy spectrum larger than the streamwise energy spectrum at $kz > 2$ (comparing the blue dashed and solid lines in Fig. 10), implying unrealistically overamplified instability development.

Using a cubic grid spacing, CM1 LES runs are capable of resolving more than 80% of the total shear stress at $z > 2\Delta z$ (Figs. 5b and 6b). Correspondingly, such LES runs predict

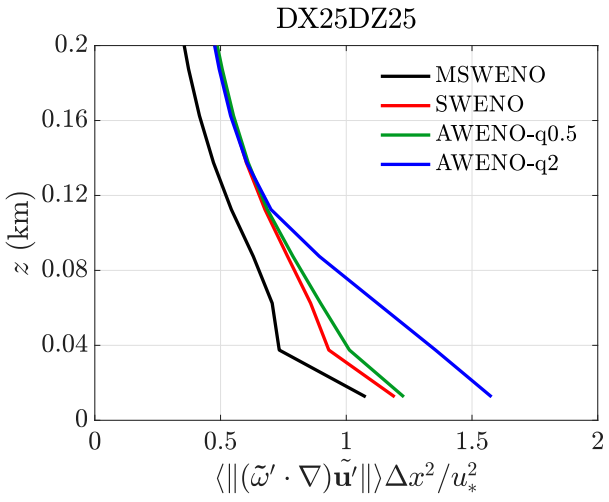

FIG. 9. Profiles of quasi-steady-state local magnitude (square norm) of turbulent vortex stretching, $\|(\tilde{\boldsymbol{\omega}}'\cdot\nabla)\tilde{\mathbf{u}}'\|$ (see Davidson 2015, chapter 4.4.1), normalized using the grid spacing and friction velocity. Results are from MSWENO-DX25DZ25, SWENO-DX25DZ25, AWENO-q0.5-DX25DZ25, and AWENO-q2-DX25DZ25 simulations and are averaged over the horizontal domain and $5 \le t \le 6$ h.

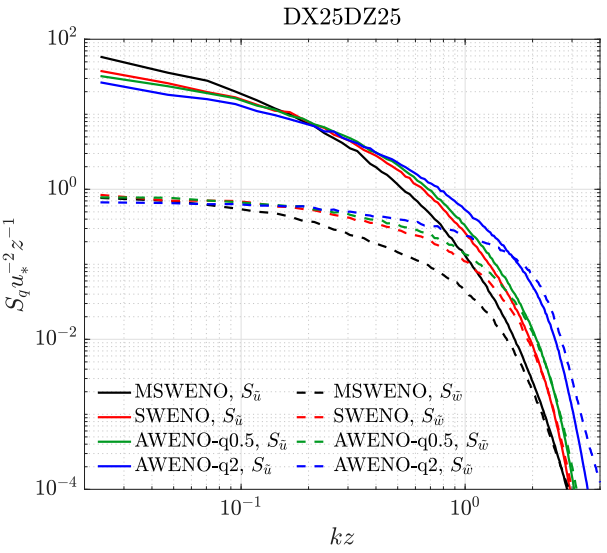

FIG. 10. The spectra of streamwise (solid lines) and vertical (dashed lines) velocity components at the second U level. Results are from MSWENO-DX25DZ25, SWENO-DX25DZ25, AWENO-q0.5-DX25DZ25, and AWENO-q2-DX25DZ25 simulations. The discrete Fourier transform is described by Stull (1988, chapter 8.4–8.6): $F_q(k) = \sum_{n=0}^{N-1}[q(n)/N]e^{-i2\pi nk/N}$, which gives the discrete spectral energy, $E_q(k) = 2 \times |F_q(k)|^2$, and then the spectral energy density, $S_q(k) = E_q(k)/\Delta k$. Here k is wavenumber, N is data length, and q is the discrete data to be transformed (e.g., $\tilde{u}$ or $\tilde{w}$). Finally, S_q is scaled by u_* and z and then averaged over $5 \le t \le 6$ h.

fairly accurate near-surface shear (Figs. 5a and 6a), leaving little room for further improvement. Nevertheless, applying AWENO schemes with $q = 0.5$ enables the best agreement between DX25DZ25 results and the filtered LOTW (comparing the green and cyan lines in Fig. 13a). Using a grid spacing of Δz finer than Δx and Δy, only 50% and 70% of the total shear stress is resolved at $z = 2\Delta z$ and $z = 3\Delta z$, respectively (Fig. 7b). Correspondingly, fairly large room for further improvement remains in the results of near-surface shear (Fig. 7a), and a relatively large q value is needed for sufficient amplification of instability development. Specifically, applying AWENO schemes with $q = 2$ yields the best agreement between DX25DZ10 results and the filtered LOTW (comparing blue and cyan lines in Fig. 14a).

In summary, by enhancing instability development and the associated energy cascade (Figs. 10 and 12), AWENO schemes are capable of increasing the ratio of resolved to total shear stress (Figs. 13b and 14b) and reducing the overprediction of near-surface shear (Figs. 13a and 14a). Similar to WENO schemes, the minor change in SGS TKE has negligible influence on the change in resolved momentum stress and nondimensional shear (Figs. 13c and 14c). The optimal choice of q value, which controls the effectiveness of AWENO schemes in amplifying instability development, depends on the grid aspect ratio ($\Delta x/\Delta z$). Using an insufficient q value is incapable of providing needed amount of energy cascade, and therefore yields little influence on near-surface shear (e.g., AWENO-q0.5-DX25DZ10 results represented by the green lines in Figs. 12 and 14). Using an excessive q value, on the other hand, may lead to underprediction of near-surface shear owning to overamplified energy cascade (e.g., AWENO-q2-DX25DZ25 results represented by the blue lines in Figs. 10 and 13). The current application of AWENO schemes to momentum advection is limited to a handful of LES configurations and prescribed constant q values. Preliminary results suggest that the optimal q value is potentially connected to a collapse of streamwise and vertical energy spectra at $kz > 2$ (see the green lines in Fig. 10 and the blue lines in Fig. 12). Such potential connection is consistent with the theoretical expectation that the choice of q value should depend on at least the resolved and SGS partitioning of the total shear stress, which is affected by energy distribution across scales.

5. Conclusions

CM1 LES results of a quasi-steady, horizontally homogeneous, fully developed, neutral ABL are used to explore the influence of WENO schemes on turbulence. Applying WENO schemes to scalar advection eliminates the propagation of acoustic waves generated by solving the compressible fluid equations and the associated high-frequency oscillations of domain-total vertical velocity. This advantage of applying WENO schemes to scalar advection, in addition to the other known advantages (e.g., allowing the use of coarse grid spacing without inducing spurious oscillations, as aforementioned in section 2b), suggests that one should employ WENO schemes for scalar advection when conducting CM1 simulations (both dry and moist). This recommendation is likely applicable to any atmospheric code solving compressible flow equations or handling moist processes.

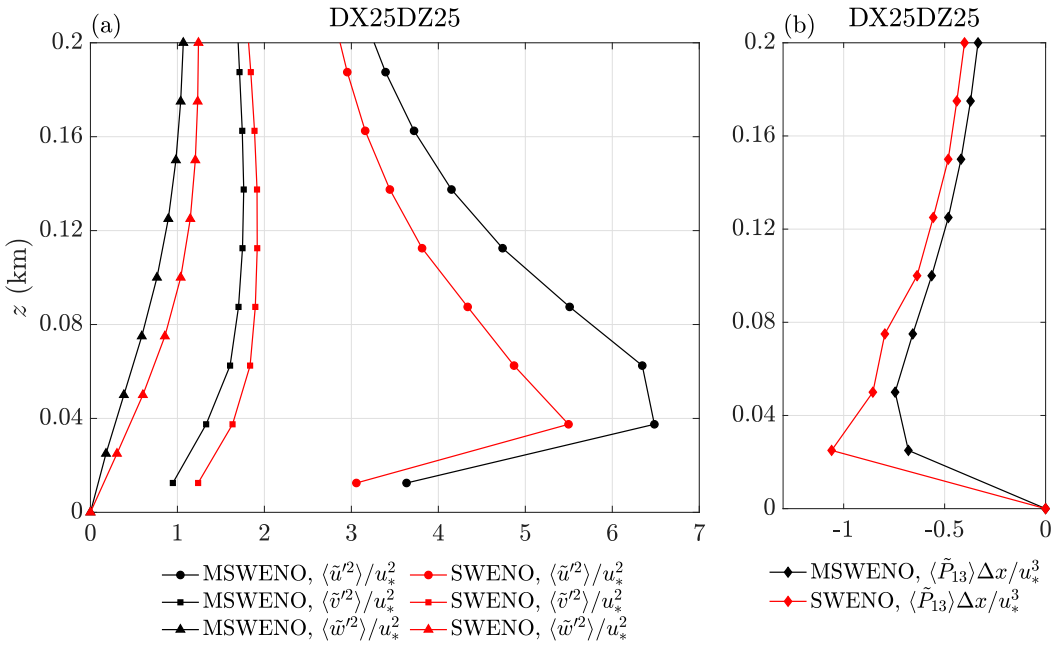

FIG. 11. Profiles of (a) quasi-steady-state resolved velocity variances and (b) the shear production of resolved Reynolds stress normalized using friction velocity and grid spacing. Results are from MSWENO-DX25DZ25 and SWENO-DX25DZ25 simulations and are averaged over the horizontal domain and $5 \le t \le 6$ h.

Applying WENO schemes to momentum advection in addition to scalar advection does not yield any further advantage, but an adverse effect on CM1 LES results of resolved turbulence. In short, WENO schemes suppress instability development, reducing turbulent vortex stretching, suppressing energy cascade, reducing shear production of resolved Reynolds stress, and eventually amplifies the deviation between LES results of surface-layer turbulence and the filtered LOTW (known as the log-layer mismatch). Thus, applying WENO schemes to momentum advection is not recommended for CM1 LES, or any turbulence-resolving simulations of low-Mach-number flows.

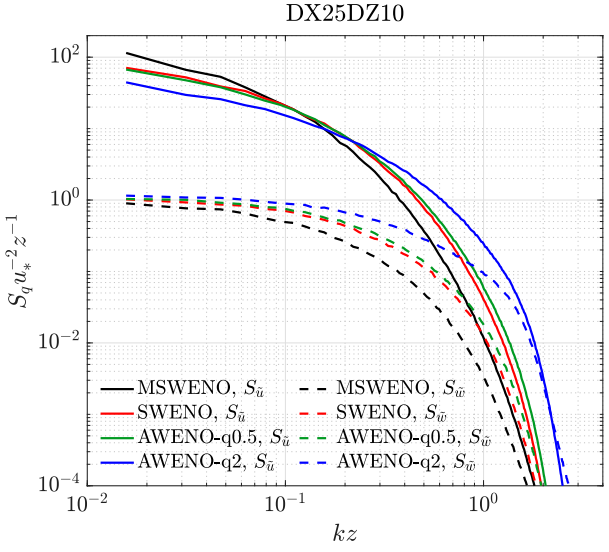

FIG. 12. As in Fig. 10 except that the velocities are from the third U level in MSWENO-DX25DZ10, SWENO-DX25DZ10, AWENO-q0.5-DX25DZ10, and AWENO-q2-DX25DZ10.

The log-layer mismatch is an example of the "terra incognita" problems described by Wyngaard (2004), where energy-containing turbulent motions are inadequately resolved by LES grids. Previous studies have explored various routes toward reproducing near-surface turbulence, including SGS models (e.g., Sullivan et al. 1994; Bou-Zeid et al. 2005; Chow et al. 2005), lower boundary conditions (e.g., Bou-Zeid et al. 2005; Kawai and Larsson 2012; Yang et al. 2017), and additional sources of surface stress (Chow et al. 2005). Although LOTW can be reproduced by modifying either SGS models or advection schemes, the success along one route does not invalidate the effort along the other route. Physically, the rate of energy dissipation determined by SGS models and the energy cascade governed by advection schemes are different quantities, where one cannot fully represent the other. An advantage of AWENO schemes is the use of first- and second-order derivatives of resolved velocity across multiple grid points to compute the stress tensor, as opposed to eddy-viscosity type of SGS models where the stress tensor is the first-order derivative of resolved velocity at a single grid point multiplied by a scalar. In other words, AWENO schemes are capable of accounting for the anisotropic and nonlocal features of the stress–strain-rate relationship in "terra incognita" problems (Wyngaard 2004). Thus, AWENO schemes are an attractive route toward

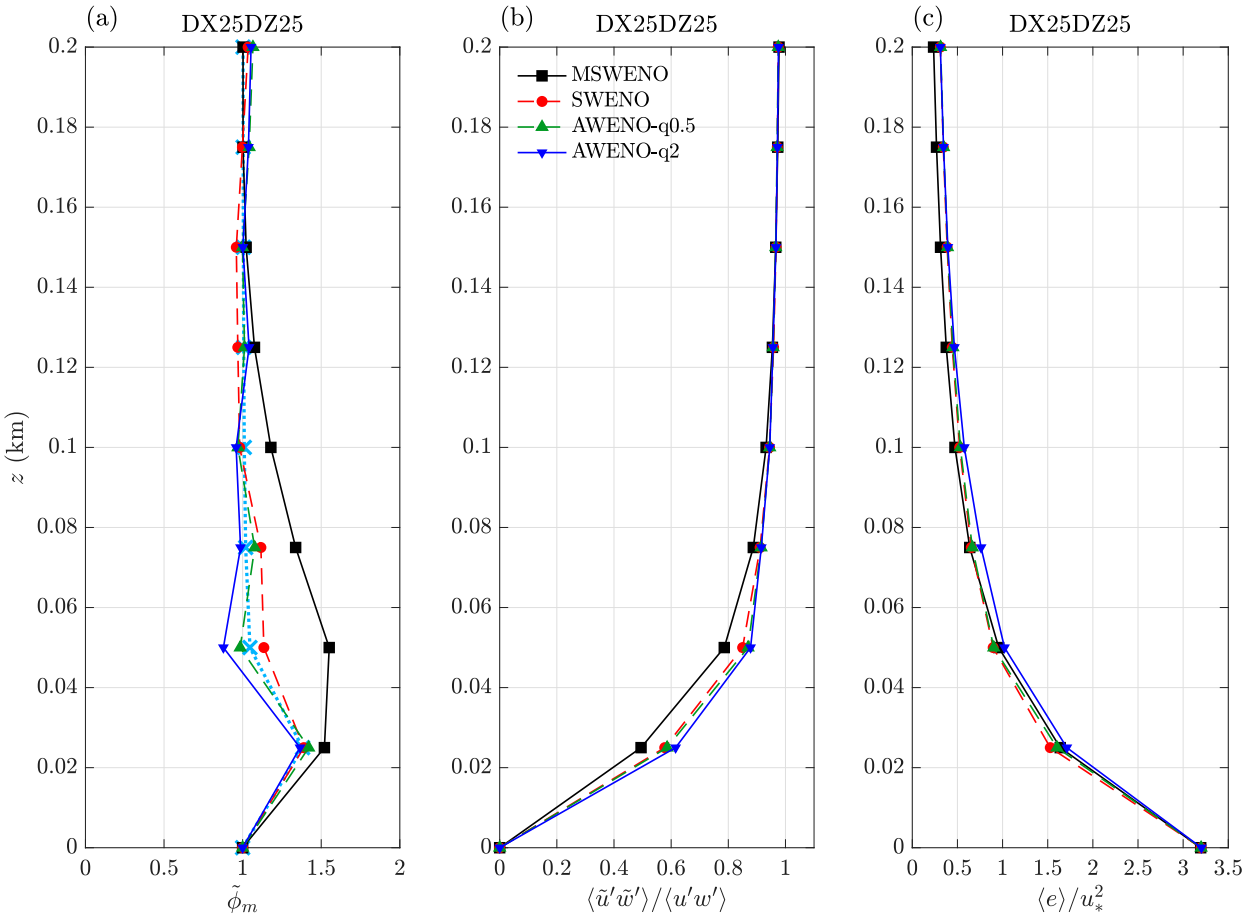

FIG. 13. As in Fig. 5, except that results are from MSWENO-DX25DZ25, SWENO-DX25DZ25, AWENO-q0.5-DX25DZ25, and AWENO-q2-DX25DZ25.

further improvements of LES models. Future work includes testing AWENO schemes with various LES configurations and exploring the physical interpretation of parameter values. In addition, the energy cascade governed by advection schemes and the dissipation computed by SGS models are connected through the energy budget equation. Thus, understanding the interactions between advection schemes and SGS models is essential for improving LES models.

Acknowledgments. We thank Min-Jhe Lu, Dr. Chau Lam Yu, Dr. George Bryan, and Dr. Xiang Yang for discussions of WENO schemes. Special thanks go to Dr. George Bryan for his continued support of CM1. This work was funded by NSF Award AGS-1821885. We would like to acknowledge high-performance computing support from Cheyenne (doi:10.5065/D6RX99HX) provided by NCAR's Computational and Information Systems Laboratory, sponsored by the National Science Foundation. Computations for this research were also performed on the Pennsylvania State University's Institute for Computational and Data Sciences' Roar supercomputer. Finally, we thank the editor, Dr. Elie Bou-Zeid, and three anonymous reviewers for their constructive comments to help us improve this paper.

Data availability statement. All numerical code and simulation outputs created in this work are openly available from the Penn State DataCommons at https://doi.org/10.26208/f8n2-3x91.

APPENDIX A

The Fifth-Order Advection and WENO Schemes

a. *The fifth-order advection scheme*

In CM1, the resolved flux of an arbitrary variable ψ is computed as

$$\left.\frac{\partial u\psi}{\partial x}\right|_{x=x_i} = \frac{1}{\Delta x}(u_{i+1/2}\psi_{i+1/2} - u_{i-1/2}\psi_{i-1/2}), \tag{A1}$$

where u is the velocity component along an arbitrary direction x. Because CM1 uses a C grid (Arakawa and Lamb 1977), one needs to compute $\psi_{i\pm1/2}$ for using grid-filtered values of variable ψ.

Given a direction x, the relationship between $\psi(x)$ and its filtered grid value $\tilde{\psi}(x)$ is

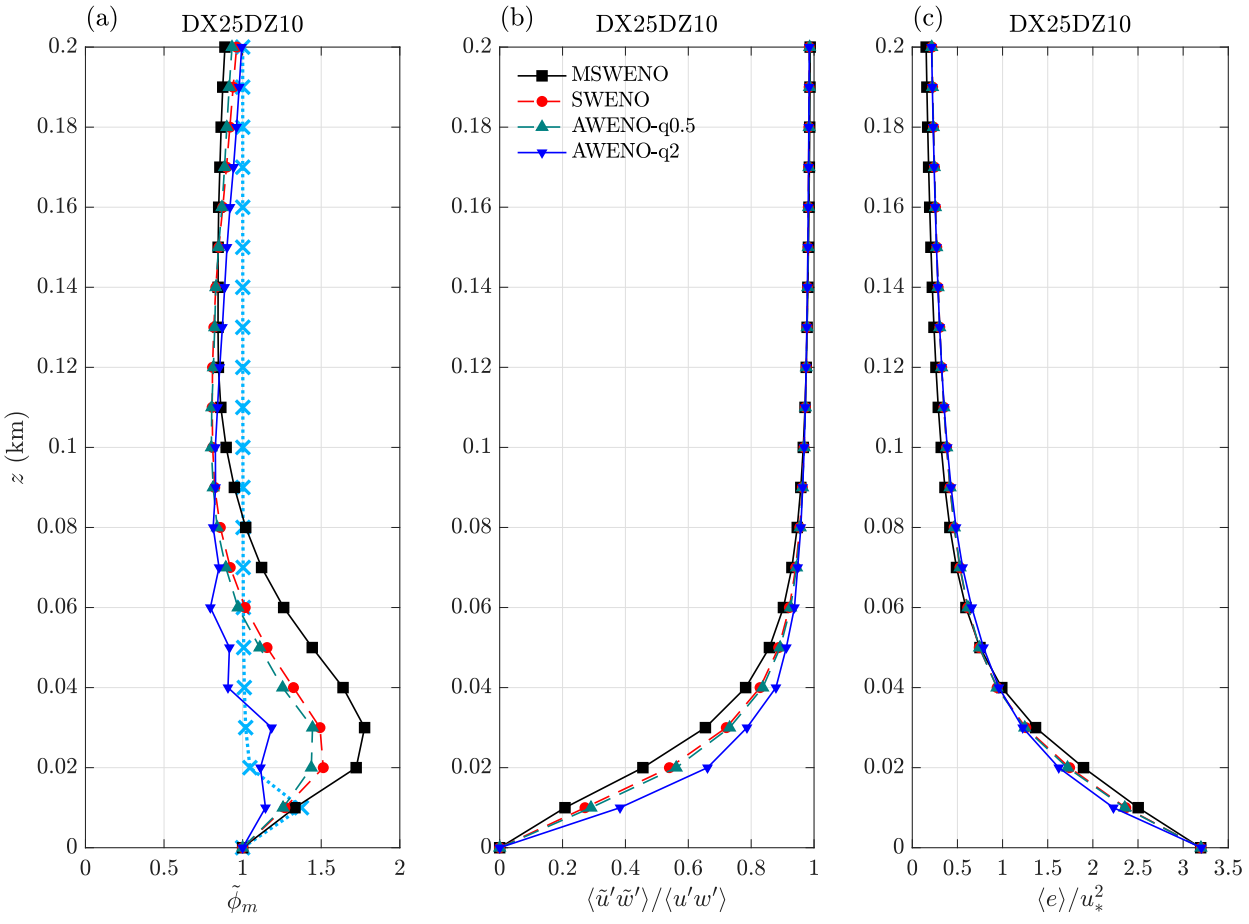

FIG. 14. As in Fig. 7, except that results are from MSWENO-DX25DZ10, SWENO-DX25DZ10, AWENO-q0.5-DX25DZ10, and AWENO-q2-DX25DZ10.

$$\tilde{\psi}(x) = \frac{1}{\Delta x}\int_{x-\Delta x/2}^{x+\Delta x/2} \psi(x')\, dx', \tag{A2}$$

which can also be viewed as $\tilde{\psi}(x)$ being the moving average of $\psi(x)$. For a fifth-order upstream scheme [also known as fifth-order Quadratic Upstream Interpolation for Convective Kinematics scheme (QUICK_5); Sanderson and Brassington 1998], at $x = x_{i\pm1/2}$, $\psi(x)$ can be approximated as $\hat{\psi}(x)$ composed of five filtered grid values $\tilde{\psi}$ via Taylor expansions (see detailed derivation of $\hat{f}$ in section 2.3 of Henrick et al. 2005):

$$\begin{aligned}
\hat{\psi}_{i+1/2} &= \frac{1}{60}(2\tilde{\psi}_{i-2} - 13\tilde{\psi}_{i-1} + 47\tilde{\psi}_i + 27\tilde{\psi}_{i+1} - 3\tilde{\psi}_{i+2}) \\
&= \psi_{i+1/2} - \frac{1}{60}\frac{d^5\tilde{\psi}}{dx^5}\bigg|_{x=x_i} \Delta x^5 + O(\Delta x^6), \\
\hat{\psi}_{i-1/2} &= \frac{1}{60}(2\tilde{\psi}_{i-3} - 13\tilde{\psi}_{i-2} + 47\tilde{\psi}_{i-1} + 27\tilde{\psi}_i - 3\tilde{\psi}_{i+1}) \\
&= \psi_{i-1/2} - \frac{1}{60}\frac{d^5\tilde{\psi}}{dx^5}\bigg|_{x=x_i} \Delta x^5 + O(\Delta x^6).
\end{aligned} \tag{A3}$$

Plugging (A3) into (A1) yields a spatial derivation approximation that is of a fifth-order accuracy,

$$\begin{aligned}
\frac{\partial\tilde{\psi}}{\partial x}\bigg|_{x=x_i} &= \frac{1}{60\Delta x}(-2\tilde{\psi}_{i-3} + 15\tilde{\psi}_{i-2} - 60\tilde{\psi}_{i-1} \\
&\quad + 20\tilde{\psi}_i + 30\tilde{\psi}_{i+1} - 3\tilde{\psi}_{i+2}) + O(\Delta x^5) \\
&= \frac{1}{\Delta x}(\hat{\psi}_{i+1/2} - \hat{\psi}_{i-1/2}) + O(\Delta x^5).
\end{aligned} \tag{A4}$$

b. *The fifth-order WENO scheme*

The fifth-order advection scheme described above will generate spurious oscillations in the presence of gradients of ψ, which are too sharp to be resolved by the grids. WENO schemes of the same order have thus been developed to reduce such spurious oscillations (Jiang and Shu 1996; Henrick et al. 2005; Borges et al. 2008).

The fifth-order WENO scheme separates the grid points for $\hat{\psi}_{i\pm1/2}$ into three stencils with three components in each stencil. Each mth stencil (S_m) contains a weight ω_m and a combination set $\hat{\psi}^m$,

$$\hat{\psi}_{i\pm1/2} = \sum_{m=0}^{2} S_m = \sum_{m=0}^{2} \omega_m \hat{\psi}^m(x_{i\pm1/2}), \tag{A5}$$

and each $\hat{\psi}^m$ contains three gridpoint values $\tilde{\psi}$. Take the one at $i + 1/2$ as an example,

$$\hat{\psi}^m_{i+1/2} = \sum_{n=0}^{2} c_{mn}\tilde{\psi}_{i+m-2+n}, \tag{A6}$$

where m denotes the index of the stencils, n denotes the index of the elements in each stencil, and the coefficient c_{mn} is listed in Table I of Jiang and Shu (1996). The weight is defined as

$$\omega_m = \frac{\alpha_m}{\sum_{l=0}^{2}\alpha_l}, \qquad \alpha_m = \frac{d_m}{(\beta_m+\epsilon)^2}, \tag{A7}$$

where d_m is called identical weight ($d_0 = 1/10$, $d_1 = 3/5$, $d_2 = 3/10$), which returns to the fifth-order upstream centered scheme when all of the weights are identical; ϵ is just a parameter used to avoid a division by zero (set as 10^{-16} in CM1 and in this current study); β_m is the smoothness indicator, which is small when the first and second derivatives are small (i.e., when the change of ψ in that $\hat{\psi}^m$ is small):

$$\beta_m = \sum_{l=1}^{2}\Delta x^{2l-1}\int_{x_{i-1/2}}^{x_{i+1/2}}\left[\frac{d^l}{dx^l}\hat{\psi}^m(x)\right]^2 dx. \tag{A8}$$

The expression of β_m by the grid values $\tilde{\psi}$ are

$$\begin{aligned}
\beta_0 &= \frac{13}{12}(\tilde{\psi}_{i-2} - 2\tilde{\psi}_{i-1} + \tilde{\psi}_i)^2 + \frac{1}{4}(\tilde{\psi}_{i-2} - 4\tilde{\psi}_{i-1} + 3\tilde{\psi}_i)^2,\\
\beta_1 &= \frac{13}{12}(\tilde{\psi}_{i-1} - 2\tilde{\psi}_i + \tilde{\psi}_{i+1})^2 + \frac{1}{4}(\tilde{\psi}_{i-1} - \tilde{\psi}_{i+1})^2,\\
\beta_2 &= \frac{13}{12}(\tilde{\psi}_i - 2\tilde{\psi}_{i+1} + \tilde{\psi}_{i+2})^2 + \frac{1}{4}(3\tilde{\psi}_i - 4\tilde{\psi}_{i+1} + \tilde{\psi}_{i+2})^2.
\end{aligned} \tag{A9}$$

Because this is an upstream scheme, so the approximation above is at $x = x_{i+1/2}$ when $\tilde{u}_{i+1/2} > 0$. The approximation at $x = x_{i-1/2}$ can be derived similarly by shifting the indices one grid lower. For example, the flux at $x = x_{i-1/2}$ and $\tilde{u}_{i-1/2} > 0$, the inputs are ($\tilde{\psi}_{i-3}$, $\tilde{\psi}_{i-2}$, $\tilde{\psi}_{i-1}$, $\tilde{\psi}_i$, $\tilde{\psi}_{i+1}$); if $\tilde{u}_{i-1/2} < 0$, the inputs become ($\tilde{\psi}_{i+2}$, $\tilde{\psi}_{i+1}$, $\tilde{\psi}_i$, $\tilde{\psi}_{i-1}$, $\tilde{\psi}_{i-2}$).

When a stencil ($\hat{\psi}^m$) involves sharp gradients of ψ, β_m will be relatively large, meaning that the weight (ω_m) becomes small, which leads to a smoothing effect and thus suppresses the generation of spurious oscillations. CM1 applies an improved version called WENO-Z (Borges et al. 2008), where

$$\begin{aligned}
\tau_5 &= |\beta_0 - \beta_2|,\\
\omega_k^z &= \frac{\alpha_k^z}{\sum_{l=0}^{2}\alpha_l^Z},\\
\alpha_k^z &= \frac{d_k}{\beta_k^z} = d_k\left[1 + \left(\frac{\tau_5}{\beta_k+\epsilon}\right)^q\right], \quad k = 0,1,2.
\end{aligned} \tag{A10}$$

Here the smooth indicator q is a positive parameter. Increasing the value of q increases the smoothing effect of the WENO-Z scheme. A default value of $q = 2$ is used in CM1. Compared to (A7), (A10) is capable of reducing numerical diffusion and thus improving the resolution of sharp gradients (Borges et al. 2008).

For the CM1 LES runs conducted in this work, the vertical grid points near upper and lower boundaries are sometimes insufficient to support the fifth-order WENO scheme. In such cases, CM1 employs the $\kappa = 1/3$ scheme (Koren and Beets 1996), which is also designed to reduce spurious oscillations. Examples include fluxes at the second U or W level away from the boundaries when $\tilde{w}$ is away from the boundaries and fluxes at the first U level away from the boundaries when $\tilde{w}$ is toward the boundaries. At the first U level away from the boundaries, when $\tilde{w}$ is away from the boundaries, CM1 uses a simple second-order centered difference scheme.

APPENDIX B

AWENO Schemes

In WENO schemes, each stencil's weight before normalized by the sum (α_k^z) is divided by the smoothness indicator [β_k^z, see (A10)] to reduce the influence of discontinuous stencils. On the contrary, AWENO schemes are designed to increase the influence of discontinuous stencils, so the weight is multiplied by the smoothness indicator as

$$\alpha_k^z = d_k\beta_k^z = \frac{d_k}{\left[1 + \left(\frac{\tau_5}{\beta_k+\epsilon}\right)^q\right]}, \quad k = 0,1,2. \tag{B1}$$

In contrast to (A10), increasing q enhances the turbulence-amplifying effect of AWENO schemes.

In this work, AWENO schemes are applied to only momentum advection at the W level near the surface (Table 2). At the second U and W level when $\tilde{w} > 0$ or at the first U level when $\tilde{w} < 0$, the grid points are limited, so the AWENO scheme is formulated as

$$\begin{aligned}
\beta_0 &= (\tilde{\psi}_{i-1} - \tilde{\psi}_i)^2,\\
\beta_1 &= (\tilde{\psi}_i - \tilde{\psi}_{i+1})^2,\\
\tau_3 &= |\beta_0 - \beta_1|,\\
\omega_k^z &= \frac{\alpha_k^z}{\sum_{l=0}^{2}\alpha_l^Z},\\
\alpha_k^z &= d_k\beta_k^z = \frac{d_k}{\left[1 + \left(\frac{\tau_3}{\beta_k+\epsilon}\right)^q\right]}, \quad k = 0,1,
\end{aligned} \tag{B2}$$

which is modified from a third-order WENO scheme with $d_0 = 1/3$ and $d_1 = 2/3$. At the first U level when $\tilde{w} > 0$, a centered difference is used.

REFERENCES

Arakawa, A., and V. R. Lamb, 1977: Computational design of the basic dynamical processes of the UCLA general circulation model. *Methods in Computational Physics: Advances in Research and Applications*, J. Chang, Ed., Vol. 17, Elsevier, 173–265.

Borges, R., M. Carmona, B. Costa, and W. S. Don, 2008: An improved weighted essentially non-oscillatory scheme for hyperbolic conservation laws. *J. Comput. Phys.*, **227**, 3191–3211, https://doi.org/10.1016/j.jcp.2007.11.038.

Bott, A., 1989: A positive definite advection scheme obtained by nonlinear renormalization of the advective fluxes. *Mon. Wea. Rev.*, **117**, 1006–1016, https://doi.org/10.1175/1520-0493(1989)117<1006:APDASO>2.0.CO;2.

Bou-Zeid, E., C. Meneveau, and M. B. Parlange, 2005: A scale-dependent Lagrangian dynamic model for large eddy simulation of complex turbulent flows. *Phys. Fluids*, **17**, 025105, https://doi.org/10.1063/1.1839152.

Brasseur, J. G., and T. Wei, 2010: Designing large-eddy simulation of the turbulent boundary layer to capture law-of-the-wall scaling. *Phys. Fluids*, **22**, 021303, https://doi.org/10.1063/1.3319073.

Bryan, G. H., 2017: The governing equations for CM1. UCAR Tech. Note, 24 pp., https://www2.mmm.ucar.edu/people/bryan/cm1/cm1_equations.pdf.

——, and J. M. Fritsch, 2002: A benchmark simulation for moist nonhydrostatic numerical models. *Mon. Wea. Rev.*, **130**, 2917–2928, https://doi.org/10.1175/1520-0493(2002)130<2917:ABSFMN>2.0.CO;2.

——, J. C. Wyngaard, and J. M. Fritsch, 2003: Resolution requirements for the simulation of deep moist convection. *Mon. Wea. Rev.*, **131**, 2394–2416, https://doi.org/10.1175/1520-0493(2003)131<2394:RRFTSO>2.0.CO;2.

Cheng, T., and K. Lee, 2005: Numerical simulations of underexpanded supersonic jet and free shear layer using WENO schemes. *Int. J. Heat Fluid Flow*, **26**, 755–770, https://doi.org/10.1016/j.ijheatfluidflow.2005.01.006.

Chow, F. K., R. L. Street, M. Xue, and J. H. Ferziger, 2005: Explicit filtering and reconstruction turbulence modeling for large-eddy simulation of neutral boundary layer flow. *J. Atmos. Sci.*, **62**, 2058–2077, https://doi.org/10.1175/JAS3456.1.

Davidson, P. A., 2015: *Turbulence: An Introduction for Scientists and Engineers.* Oxford University Press, 629 pp.

Deardorff, J. W., 1980: Stratocumulus-capped mixed layers derived from a three-dimensional model. *Bound.-Layer Meteor.*, **18**, 495–527, https://doi.org/10.1007/BF00119502.

Drazin, P. G., and W. H. Reid, 2004: Parallel shear flows. *Hydrodynamic Stability*, 2nd ed. Cambridge University Press, 124–250.

Henrick, A. K., T. D. Aslam, and J. M. Powers, 2005: Mapped weighted essentially non-oscillatory schemes: Achieving optimal order near critical points. *J. Comput. Phys.*, **207**, 542–567, https://doi.org/10.1016/j.jcp.2005.01.023.

Jeong, J., and F. Hussain, 1995: On the identification of a vortex. *J. Fluid Mech.*, **285**, 69–94, https://doi.org/10.1017/S0022112095000462.

Jiang, G.-S., and C.-W. Shu, 1996: Efficient implementation of weighted ENO schemes. *J. Comput. Phys.*, **126**, 202–228, https://doi.org/10.1006/jcph.1996.0130.

Kawai, S., and J. Larsson, 2012: Wall-modeling in large eddy simulation: Length scales, grid resolution, and accuracy. *Phys. Fluids*, **24**, 015105, https://doi.org/10.1063/1.3678331.

Koren, B., and C. Beets, 1996: Large-eddy simulation with accurate implicit subgrid-scale diffusion. CWI Rep. NM-R9601, 26 pp., https://ir.cwi.nl/pub/4897.

Lunet, T., C. Lac, F. Auguste, F. Visentin, V. Masson, and J. Escobar, 2017: Combination of WENO and explicit Runge–Kutta methods for wind transport in the Meso-NH model. *Mon. Wea. Rev.*, **145**, 3817–3838, https://doi.org/10.1175/MWR-D-16-0343.1.

Markowski, P. M., and G. H. Bryan, 2016: LES of laminar flow in the PBL: A potential problem for convective storm simulations. *Mon. Wea. Rev.*, **144**, 1841–1850, https://doi.org/10.1175/MWR-D-15-0439.1.

Mason, P. J., and D. J. Thomson, 1992: Stochastic backscatter in large-eddy simulations of boundary layers. *J. Fluid Mech.*, **242**, 51–78, https://doi.org/10.1017/S0022112092002271.

Pope, S. B., 2000: *Turbulent Flows.* Cambridge University Press, 771 pp.

Porté-Agel, F., C. Meneveau, and M. B. Parlange, 2000: A scale-dependent dynamic model for large-eddy simulation: Application to a neutral atmospheric boundary layer. *J. Fluid Mech.*, **415**, 261–284, https://doi.org/10.1017/S0022112000008776.

Prandtl, L., 1933: Recent results of turbulence research. NACA Tech. Memo. 720, 30 pp., https://digital.library.unt.edu/ark:/67531/metadc63523/.

Pressel, K. G., C. M. Kaul, T. Schneider, Z. Tan, and S. Mishra, 2015: Large-eddy simulation in an anelastic framework with closed water and entropy balances. *J. Adv. Model. Earth Syst.*, **7**, 1425–1456, https://doi.org/10.1002/2015MS000496.

——, S. Mishra, T. Schneider, C. M. Kaul, and Z. Tan, 2017: Numerics and subgrid-scale modeling in large eddy simulations of stratocumulus clouds. *J. Adv. Model. Earth Syst.*, **9**, 1342–1365, https://doi.org/10.1002/2016MS000778.

Sanderson, B., and G. Brassington, 1998: Accuracy in the context of a control-volume model. *Atmos.–Ocean*, **36**, 355–384, https://doi.org/10.1080/07055900.1998.9649617.

Shi, X., F. K. Chow, R. L. Street, and G. H. Bryan, 2018: An evaluation of LES turbulence models for scalar mixing in the stratocumulus-capped boundary layer. *J. Atmos. Sci.*, **75**, 1499–1507, https://doi.org/10.1175/JAS-D-17-0392.1.

Shu, C.-W., 2003: High-order finite difference and finite volume WENO schemes and discontinuous Galerkin methods for CFD. *Int. J. Comput. Fluid Dyn.*, **17**, 107–118, https://doi.org/10.1080/1061856031000104851.

Skamarock, W. C., and J. B. Klemp, 2008: A time-split nonhydrostatic atmospheric model for Weather Research and Forecasting applications. *J. Comput. Phys.*, **227**, 3465–3485, https://doi.org/10.1016/j.jcp.2007.01.037.

Stull, R. B., 1988: *An Introduction to Boundary Layer Meteorology*. Kluwer Academic, 666 pp.

Sullivan, P. P., J. C. McWilliams, and C.-H. Moeng, 1994: A subgrid-scale model for large-eddy simulation of planetary boundary-layer flows. *Bound.-Layer Meteor.*, **71**, 247–276, https://doi.org/10.1007/BF00713741.

Tennekes, H., and J. L. Lumley, 1972: *A First Course in Turbulence*. MIT Press, 300 pp.

Tremback, C. J., J. Powell, W. R. Cotton, and R. A. Pielke, 1987: The forward-in-time upstream advection scheme: Extension to higher orders. *Mon. Wea. Rev.*, **115**, 540–555, https://doi.org/10.1175/1520-0493(1987)115<0540:TFTUAS>2.0.CO;2.

Tushaus, S. A., D. J. Posselt, M. M. Miglietta, R. Rotunno, and L. D. Monache, 2015: Bayesian exploration of multivariate orographic precipitation sensitivity for moist stable and neutral flows. *Mon. Wea. Rev.*, **143**, 4459–4475, https://doi.org/10.1175/MWR-D-15-0036.1.

Wyngaard, J. C., 2004: Toward numerical modeling in the "terra incognita." *J. Atmos. Sci.*, **61**, 1816–1826, https://doi.org/10.1175/1520-0469(2004)061<1816:TNMITT>2.0.CO;2.

——, 2010: *Turbulence in the Atmosphere*. Cambridge University Press, 393 pp.

Yang, X. I., G. I. Park, and P. Moin, 2017: Log-layer mismatch and modeling of the fluctuating wall stress in wall-modeled large-eddy simulations. *Phys. Rev. Fluids*, **2**, 104601, https://doi.org/10.1103/PhysRevFluids.2.104601.